



Daily Global Sea Surface Ageostrophic Current Dataset from 1993–2023 via Physics-Informed Deep Learning

Guangxi Cui^{1,2}, Ka-Veng Yuen³, Ying Chen^{1,2}, Zhiqiang Liu⁴, Dingqi Yang⁵, Guanliang Liu^{6,7}, Zhongya Cai^{1,2*}

5 ¹State Key Laboratory of Internet of Things for Smart City, Department of Ocean Science and Technology, University of Macau, Macau, China

²Center for Ocean Research in Hong Kong and Macau (CORE), Hong Kong, China

³State Key Laboratory of Internet of Things for Smart City, Department of Civil and Environmental Engineering, University of Macau, Macau, China

10 ⁴Department of Ocean Science and Engineering and Center for Complex Flows and Soft Matter Research, Southern University of Science and Technology, Shenzhen, China

⁵State Key Laboratory of Internet of Things for Smart City, Department of Computer and Information Science, University of Macau, Macau, China

15 ⁶State Key Laboratory of Physical Oceanography, Institute of Oceanographic Instrumentation, Shandong Academy of Sciences, Jinan, China

⁷Qilu University of Technology (Shandong Academy of Sciences), Jinan, China

Correspondence to: Zhongya Cai (zycai@edu.mo)



Abstract

20 Surface ocean circulation shapes climate, air-sea exchange, and the transport of heat, carbon, and other tracers, yet most long-term satellite-based global datasets rely primarily on geostrophic balance and therefore miss important ageostrophic motions. Here, we reconstruct global daily sea surface circulation at 0.25° resolution from 1993 to 2023 using a physics-informed deep learning framework that integrates satellite altimetry with momentum constraints from geostrophic balance, wind stress, and nonlinear advection. The resulting dataset is dynamically consistent, with a mean momentum-balance error below 1.5%, and
25 reduces the median velocity error against independent mooring observations to 0.07 m s^{-1} , compared with 0.20 m s^{-1} for geostrophic currents and 0.10 m s^{-1} for Ekman-corrected currents. We show that geostrophic flow sets the large-scale circulation, whereas Ekman and nonlinear contributions are smaller but comparable in magnitude to each other. Although nonlinear advection contributes little to relative vorticity, it strongly shapes surface divergence and the fine-scale structure of eddy kinetic energy. Our results show that nonlinear ageostrophic flow is an essential component of global surface circulation
30 and that neglecting it limits our ability to resolve surface transport and variability on climatically relevant scales.

Index Term: Ageostrophic Circulation, Ekman Dynamics, Physics-Informed Dense Neural Network, Satellite Altimetry



1 Introduction

35 Surface ocean circulation regulates climate, air-sea exchange, and the transport of heat, carbon, nutrients, and other tracers. Over the past several decades, satellite remote sensing has provided the principal observational basis for studying upper-ocean circulation (Du et al., 2021; Fan et al., 2025; Shang et al., 2025). Geostrophic currents derived from sea surface height have become central to analyses of ocean dynamics (Xie et al., 2024), climate change, and ecosystem assessments (Timmermans and Marshall, 2020; Srinivasan and Tsontos, 2023). However, geostrophic currents neglect the influence of ageostrophic processes, such as wind stress and nonlinear effects (Hiron et al., 2021). Although ageostrophic processes are relatively small in magnitude, both observational data and numerical simulations have consistently shown that they substantially modulate ocean circulation (Rio et al., 2014; Edwards et al., 2024). Ageostrophic motions play a crucial role in the evolution and adjustment of ocean circulation. For example, nonlinear effects contribute to the evolution of mesoscale eddies (Li et al., 2022) and are important for the transport of heat, dissolved carbon, and tracers (Ueno et al., 2023). Studies have also shown that nonlinear processes can reduce geostrophic current speeds by more than 0.2 m s^{-1} (Cao et al., 2023b), whereas wind-driven Ekman effects can enhance sea surface current velocities (Rio et al., 2014). Neglecting ageostrophic processes (Armitage et al., 2017; Shankar et al., 2002; Cho et al., 2025) omits the complex features introduced by variations in nonlinear forcing and wind stress (Andres et al., 2008; Buckingham et al., 2021), leading to substantial discrepancies with drifter-observed velocities (Douglass and Richman, 2015; Uchida and Imawaki, 2003). This omission introduces uncertainties in understanding the long-term evolution and energy transformation of ocean circulation.

The influence of ageostrophic motions is especially pronounced in energetically active regions such as western boundary currents, the subtropical countercurrent, and the Antarctic Circumpolar Current, where their kinetic energy can be comparable to that of geostrophic motions (Zhang et al., 2019). The development of ageostrophic motions can disrupt geostrophic balance, promote forward energy transfer, and influence the inverse transfer of geostrophic energy, leading to an increase in the mean geostrophic wavenumber (Kafiabad et al., 2019; Thomas and Daniel, 2021). Ageostrophic motions are also closely linked to marine ecosystems: the intense vertical motions they induce provide an important pathway for delivering nutrients into the euphotic zone and thereby help regulate primary productivity and carbon sequestration in the global ocean (Aluie et al., 2018; Liu et al., 2025; Masuda et al., 2021).

Most existing corrections to sea surface circulation adopt a steady-state framework (Fraser et al., 2024), and two main methods are commonly used to represent nonlinear effects. One assumes axisymmetric vortices and reduces nonlinear forcing to the centrifugal term in the gradient wind equation (Ioannou et al., 2019). The other uses a perturbation expansion in which the nonlinear term is approximated by the rate of change of geostrophic velocity (Penven et al., 2014). In practice, most previous studies have used iterative schemes for circulation correction (Cao et al., 2023a; Penven et al., 2014). The iterative solution of the gradient wind equation was first developed in atmospheric science (Cao et al., 2023a; Penven et al., 2014) and later introduced into oceanography. Such schemes have been applied to a large gyre in the Mozambique Channel, mesoscale eddies in the Mediterranean Sea (Cao et al., 2023a; Penven et al., 2014; Morales-Márquez et al., 2023), and the correction of



the global sea surface circulation field (Cao et al., 2023b; Ruiz et al., 2014). However, these schemes can diverge when the gradient wind equation has no solution (Douglass and Richman, 2015; Qiu et al., 2019). Furthermore, the stopping criterion for these schemes is typically when the velocity residual either begins to diverge or decreases below a predefined threshold (Douglass and Richman, 2015; Qiu et al., 2019), which is commonly set to 0.01 m s^{-1} in the literature (Cao et al., 2023a; Arnason et al., 1962; Penven et al., 2014). As a result, the dynamical consistency of the corrected solution remains uncertain.

Recent advances in artificial intelligence (AI) have created new opportunities for oceanographic data analysis and reconstruction (Li et al., 2020; Dong et al., 2022; Qin et al., 2023; Cui et al., 2025). AI has been applied to infer ocean surface dynamic parameters and structures (Bonino et al., 2024; Jang et al., 2022; Lenain et al., 2026; Su et al., 2026), such as subsurface eddy kinetic energy (Xie et al., 2024), subsurface thermohaline structure (Zhou et al., 2024), and sea surface temperature (Bonino et al., 2024; Kumar et al., 2021; Kartal, 2023). AI-based research on sea surface circulation is also beginning to emerge. Existing work primarily uses machine learning to replace traditional geostrophic relationships by combining satellite-observed variables, such as sea surface height, sea surface temperature, and wind stress, to reconstruct global sea surface circulation fields (Sinha and Abernathy, 2021; Manucharyan et al., 2021). However, these approaches do not fully integrate the governing physical equations of ocean surface circulation into the learning framework for ageostrophic correction. As a result, the reconstructed flow fields can retain non-negligible dynamical imbalances, as reflected in residual terms of the momentum equations.

Here, we develop a physics-informed dense neural network with ageostrophic circulation correction (AC-PIDNN) to reconstruct global sea surface circulation while explicitly enforcing momentum balance. The model integrates constraints from geostrophic balance, wind stress, and nonlinear advection to recover ageostrophic flow from satellite-observed sea surface height gradients. Using the AC-PIDNN, we generate a daily global ageostrophic current dataset from 1993 to 2023 at a spatial resolution of 0.25° . This framework enables a dynamically consistent assessment of how ageostrophic processes shape global surface circulation, divergence, and eddy energetics. The structure of this paper is as follows: Section 2 describes the data used; Section 3 introduces the proposed methodology; Section 4 presents the experimental results and discussions; Sections 5 and 6 present the code and data availability and conclusions, respectively.

2 Data

2.1 Satellite Data

The dataset used in this study includes the daily Absolute Dynamic Topography (ADT) gridded data, geostrophic currents u_g and v_g , and the corresponding surface Ekman components of the global ocean, which were downloaded from <https://data.marine.copernicus.eu/product>. The ADT gridded data are provided by the French Space Agency (CNES) through the Archiving, Validation, and Interpretation of Satellite Oceanographic data (AVISO) service, and are processed by the CNES/CLS Data Unification and Altimeter Combination System (DUACS). This system integrates observations from all Sentinel altimetry missions as well as other collaborative or opportunistic missions. The datasets incorporate high-quality



altimeter measurements and geophysical corrections and are generated using a consistent correction system to ensure maximum data quality and to minimize temporal artifacts. This dataset also provides geostrophic currents u_g and v_g based on the geostrophic balance. These data used in this study have a temporal resolution of 1 day and a spatial resolution of $1/4^\circ$.

The surface Ekman components are obtained from the global Copernicus Ocean (GLOBCURRENT) surface and 15-meter Ekman and geostrophic current datasets. These data are derived by applying an empirical Ekman model to ERA5 wind stress fields (Mulet et al., 2021; Rio et al., 2014), with the calculation taking into account both wind stress and the mixed layer depth. The inclusion of mixed layer depth reflects the dynamic variability of Ekman depth across time and space. This product provides datasets on a $1/4^\circ$ regular grid, offering current velocity fields at the surface and at 15 m depth with hourly, daily, and monthly temporal resolutions.

2.2 Simulation Data

To validate the performance of the method proposed in this study, we conducted a high-resolution numerical simulation using the Regional Ocean Modeling System (ROMS) (Shchepetkin and McWilliams, 2005). The simulation results served as the “ground truth” for assessing the accuracy of our approach. ROMS is a widely used, high-resolution numerical framework designed for simulating regional-scale oceanic and atmospheric processes. By solving the governing equations of fluid motion, ROMS provides accurate simulations of ocean circulation, temperature, salinity, and other essential physical properties while maintaining strong dynamical consistency and numerical stability. In this study, the simulation configuration covers the western Pacific region (5°N – 32°N , 109°E – 141°E) with a spatial resolution of 3 km. The output is provided as a 30-day mean field. This high-resolution setup effectively resolves mesoscale and submesoscale oceanic dynamical processes, thereby establishing a reliable and physically consistent numerical benchmark for evaluating the accuracy and effectiveness of our method. It also forms a foundation for further investigation of regional circulation characteristics and underlying dynamical mechanisms.

120 3 Methodology

3.1 The Steady State Momentum Balance Equations

In this study, the surface sea currents within the Ekman layer are assumed satisfy the steady state momentum balance between nonlinear advection, pressure gradient force, Coriolis force and wind stress (Sudre et al., 2013; Van Meurs and Niiler, 1997):

$$125 \quad \overbrace{u \frac{\partial u}{\partial x} + v \frac{\partial u}{\partial y}}^{ADV_x} = \overbrace{\widetilde{f}v}^{COR_x} - \overbrace{g \frac{\partial \eta}{\partial x}}^{PGF_x} + \overbrace{\frac{1}{h_e} \left(\frac{\tau_x}{\rho} - r_e u_e \right)}^{WIND_x} \quad (1)$$



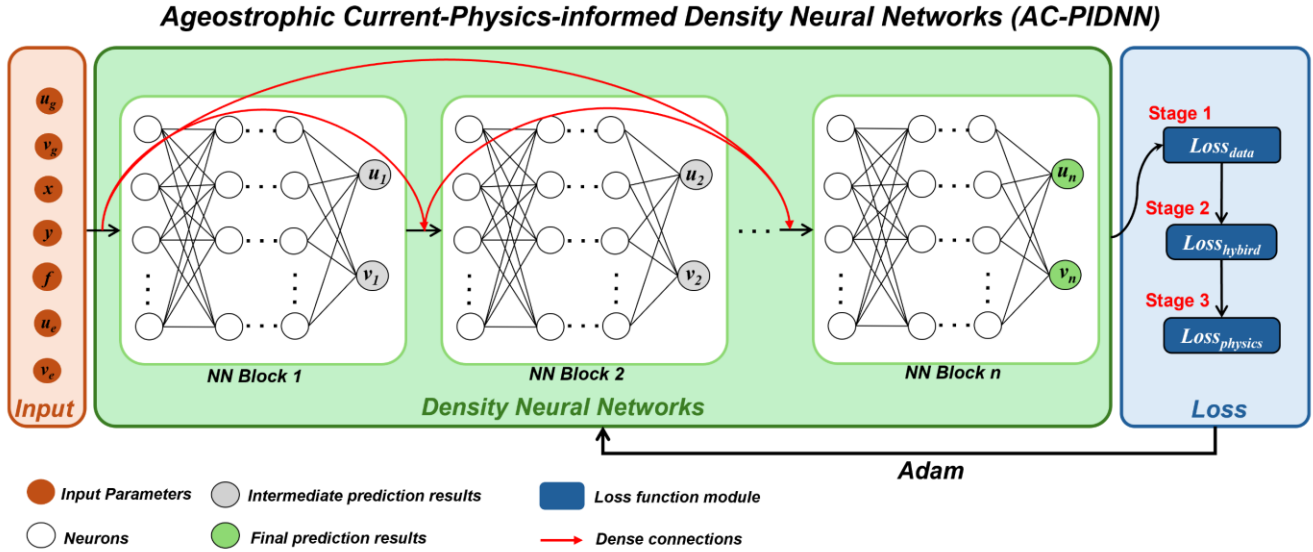
$$\overbrace{u \frac{\partial v}{\partial x} + v \frac{\partial v}{\partial y}}^{ADV_y} = \overbrace{-fu}^{COR_y} - g \overbrace{\frac{\partial \eta}{\partial y}}^{PGF_y} + \overbrace{\frac{1}{h_e} \left(\frac{\tau_y}{\rho} - r_e v_e \right)}^{WIND_y} \quad (2)$$

where, u and v are the zonal and meridional velocities; η is the sea surface height from ADT data; f represents the Coriolis force parameter; g is gravity acceleration; and $\tau(\tau_x, \tau_y)$ is the wind stress field. The h_e and r_e are thickness of the Ekman layer and the linear drag coefficient that represents the vertical viscosity terms as a body force on the Ekman components. With the information from the locally estimated h_e and r_e , the u_e and v_e can be calculated based on the wind stress field. In our

130 calculation, the $\overbrace{\frac{1}{h_e} \left(\frac{\tau_x}{\rho} - r_e u_e \right)}^{WIND_x}$ and $\overbrace{\frac{1}{h_e} \left(\frac{\tau_y}{\rho} - r_e v_e \right)}^{WIND_y}$ are represented by the $-fv_e$ and fu_e , in which u_e and v_e are the Ekman component of current in GLOBCURRENT data to simplify the calculation.

3.2 Physics-informed Density Neural Networks for Correcting Ageostrophic Current (AC-PIDNN)

135 In this study, we propose a physics-informed neural network (PINN)-based architecture for correcting ageostrophic current, termed AC-PIDNN. The overall structure, as shown in Figure 1, consists of four components: input module, custom density neural networks module, and loss function module.



Loss function in three stages of training

$$\text{Stage 1} \quad Loss_{data} = \frac{1}{N} \sum_{i=1}^N |u_g - u_i|^2 + |v_g - v_i|^2$$

$$\text{Stage 2} \quad Loss_{hybrid} = \frac{1}{N} \sum_{i=1}^N |ADV_x + COR_x + PGF_x + WIND_x|^2 + |ADV_y + COR_y + PGF_y + WIND_y|^2 + \frac{1}{N} \sum_{i=1}^N |u_g - u_i|^2 + |v_g - v_i|^2$$

$$\text{Stage 3} \quad Loss_{physics} = \frac{1}{N} \sum_{i=1}^N |ADV_x + COR_x + PGF_x + WIND_x|^2 + |ADV_y + COR_y + PGF_y + WIND_y|^2$$

Figure 1: Schematic diagram of the proposed sea surface circulation correction model (AC-PIDNN).

3.2.1 Input Module

140 The model inputs include geostrophic current components derived from the geostrophic approximation (u_g, v_g), surface Ekman current components (u_e, v_e), Coriolis parameter f , and geographical coordinates (x, y). The input features be represented as:

$$\mathbf{X} = [u_g, v_g, x, y, f, u_e, v_e] \quad (3)$$

The geostrophic currents are calculated based on the geostrophic balance:

145
$$f v_g - g \frac{\partial \eta}{\partial x} = 0 \quad (4)$$

$$-f u_g - g \frac{\partial \eta}{\partial y} = 0 \quad (5)$$

However, Equations (4) and (5) become singular at the equator ($f = 0$), and they are also problematic in its vicinity due to the weak Coriolis effect. To address this issue, within the latitude band of $\pm 2^\circ$, this study adopts the so-called “semi-geostrophic”



approximation to compute the equatorial current components (u_{sg}, v_{sg}), which replace the geostrophic currents in this region
150 (Sudre et al., 2013):

$$u_{sg} = -\frac{g}{\beta} \frac{\partial^2 \eta}{\partial y^2} \quad (6)$$

$$v_{sg} = \frac{g}{\beta} \frac{\partial^2 \eta}{\partial x^2} \quad (7)$$

where β is the meridional gradient of the Coriolis parameter, defined as $\beta = \frac{2\Omega \cos \varphi}{R}$, Ω is the Earth's angular velocity of rotation, φ is the latitude, R is the Earth's radius.

155 3.2.2 Density Neural Networks Module

The Density Neural Networks module incorporates multiple fully connected neural network (NN) layers, organized into NN submodules, and employs residual connections similar to ResNet (**Error! Reference source not found.**) to facilitate efficient information transfer between modules. This design aims to minimize the loss of information from the initial geostrophic current field during feature extraction and to accelerate model convergence and enhance stability. The AC-PIDNN
160 architecture employs three NN blocks, each containing five hidden layers with 100 neurons per layer. Each NN block consists of a sequence of fully connected transformations:

$$h^{(l)} = \sigma(W^{(l)}h^{(l-1)} + b^{(l)}), \quad l = 1, \dots, L \quad (8)$$

where $\mathbf{h}^{(0)} = \mathbf{X}$, $W^{(l)}$ and $b^{(l)}$ are the trainable weights and biases of the l -th layer, $\sigma(\cdot)$ denotes the activation function, and L is the number of hidden layers in each block. To preserve the physical meaning of the geostrophic input and reduce the loss of
165 dynamical information, a residual connection is applied:

$$h^{(l)} = f(h^{(l)}) + h^{(l-1)} \quad (9)$$

This residual mechanism allows the NN block to learn corrections to the geostrophic current field rather than re-learning it from scratch. From a physical perspective, the predicted current field (u, v) can be expressed as the sum of the geostrophic component and a correction term:

$$170 \quad u = u_g + \Delta u(\mathbf{X}; \theta) \quad (10)$$

$$v = v_g + \Delta v(\mathbf{X}; \theta) \quad (11)$$

where Δu and Δv are the data-driven corrections parameterized by the network weights θ . This formulation ensures that the essential dynamical information from the geostrophic approximation is retained while enabling the network to learn the ageostrophic corrections. Consequently, the residual structure accelerates convergence, improves gradient stability during
175 backpropagation, and prevents the model from overfitting to spurious patterns in the training data.



3.2.3 Loss Function Module and Training Strategy

The loss function module consists of three customized loss functions:

$$Loss_{data} = \frac{1}{N} \sum_{i=1}^N \|u_g - u_i\|^2 + \|v_g - v_i\|^2 \quad (12)$$

$$Loss_{physics} = \frac{1}{N} \sum_{i=1}^N \|ADV_x + COR_x + PGF_x + WIND_x\|^2 + \|ADV_y + COR_y + PGF_y + WIND_y\|^2 \quad (13)$$

$$Loss_{hybird} = Loss_{data} + Loss_{physics} \quad (14)$$

180

Here, N denotes the number of training samples; (u_g, v_g) represent the geostrophic current components computed under geostrophic balance; and (u_i, v_i) are the model-predicted current components; $Loss_{data}$ represents the mean squared error between the predicted and geostrophic currents, and is used for initial model fitting; $Loss_{physics}$ measures the residuals of the predicted current field in the momentum equations, constraining the outputs to satisfy the two-dimensional momentum balance as closely as possible; It is worth noting that the $Loss_{physics}$ is calculated for each predicted (u_i, v_i) , which is a dynamic value. $Loss_{hybird}$ is a weighted combination of the above two, enabling a smooth transition from data-driven to physics-driven learning by gradually increasing the weight of physical constraints during training.

185

The adaptive optimization algorithm Adam (Kingma and Ba, 2014) is employed to minimize the loss function, and neural network parameters are initialized using the Xavier scheme (Glorot and Bengio, 2010). Once training converges and the loss function reaches a sufficiently small value, the predicted (u, v) values approximate the solutions of the momentum equations (1) and (2). To ensure stability and accuracy, a three-stage training strategy is adopted:

190

Stage 1: Train with $Loss_{data}$ only, using a learning rate of 0.001 and epoch=1000, to quickly fit the geostrophic current field and initialize network weights.

195

Stage 2: Train with $Loss_{hybird}$, using a learning rate of 0.0001 and epoch=1000, to gradually introduce physical constraints and avoid gradient instability or entrapment in poor local minima caused by strong constraints in the early stage.

Stage 3: Train with $Loss_{physics}$ only, using a learning rate of 0.00001 and epoch=10000, to minimize the residuals of the momentum equations and obtain high-accuracy solutions that satisfy the physical balance as closely as possible.

3.3 Ageostrophic Current Component Decomposition

200

The ocean current field V_{total} predicted by PINN contains the component of geostrophy (\vec{V}_{geo}), wind stress (\vec{V}_{Ekman}), and nonlinearity (\vec{V}_{adv}):

$$\vec{V}_{total} = \vec{V}_{geo} + \vec{V}_{adv} + \vec{V}_{Ekman} \quad (15)$$



Where \vec{V}_{total} is the velocity vector predicted by AC-PIDNN, \vec{V}_{geo} is the geostrophic current from AVISO data and \vec{V}_{Ekman} is surface Ekman current in GLOBCURRENT data. Thus, the ADV, COR and WIND effect in Equation (1-2) is represented as $f\vec{k} \times \vec{V}_{adv}$, $f\vec{k} \times \vec{V}_{total}$, and $f\vec{k} \times \vec{V}_{Ekman}$.

205 To verify the balance of the predicted u and v from PINN, the following balance was examined:

$$Bal_x = COR_x + PGF_x + WIND_x + ADV_x \quad (16)$$

$$Bal_y = COR_y + PGF_y + WIND_y + ADV_y \quad (17)$$

$$Bal = \left(\left(\frac{Bal_x}{PGF_x} \right)^2 + \left(\frac{Bal_y}{PGF_y} \right)^2 \right)^{\frac{1}{2}} \quad (18)$$

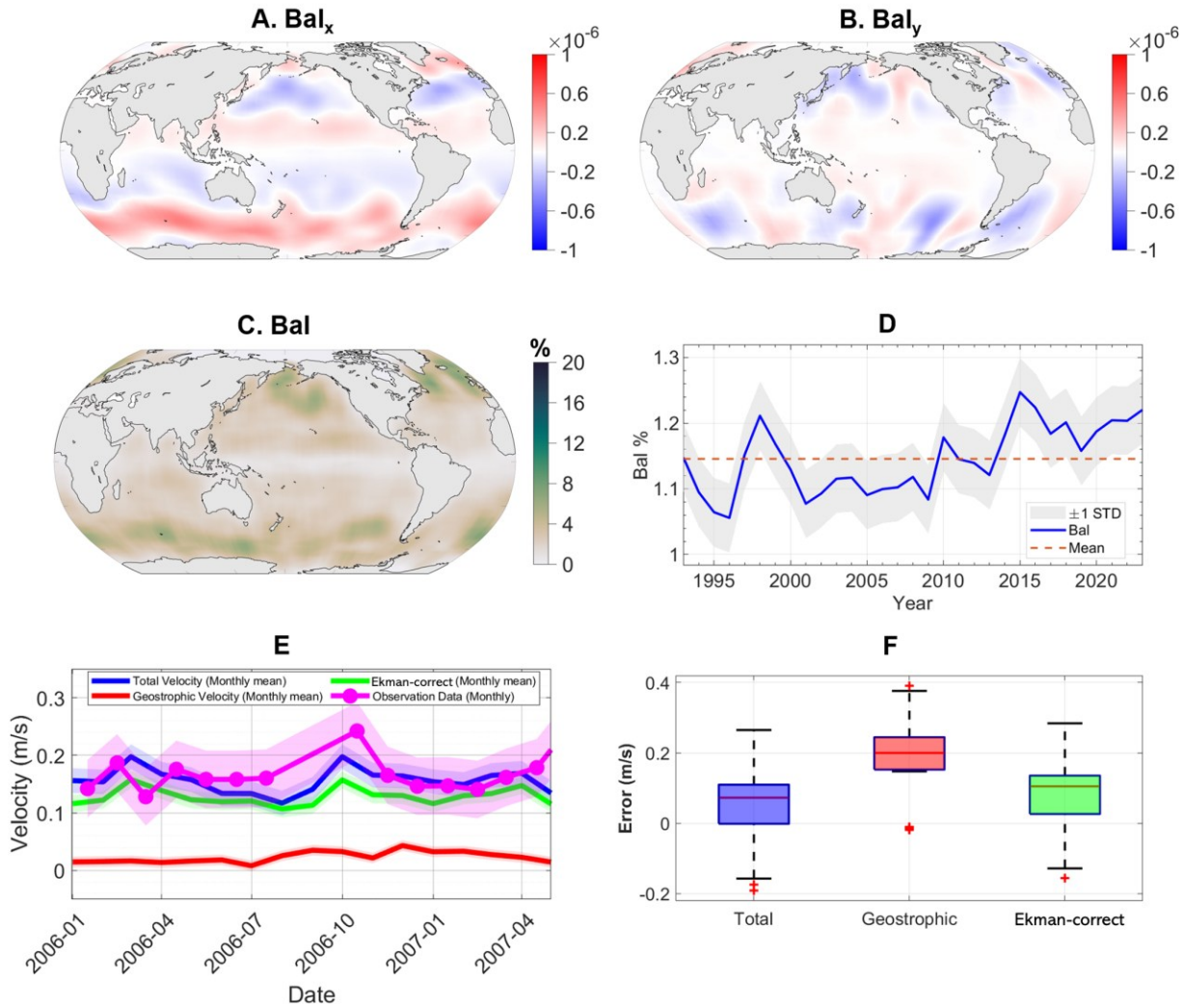
Which quantifies the normalized residual of the balance in Equation (1-2).

210 4 Results and Discussions

4.1 Validation of reconstructed currents and dynamical consistency

This study employed the AC-PIDNN to reconstruct the daily global sea surface circulation from 1993 to 2023, incorporating geostrophic, nonlinear advective and Ekman components. The 30-year mean dynamical consistency of the AC-PIDNN-reconstructed surface circulation was evaluated by examining the zonal (Bal_x) and meridional (Bal_y) balances, together with the ratio of the residual magnitude to the pressure gradient force (Bal) (Fig.2 (a-c)). The residuals are generally small over most of the global ocean, with typical magnitudes on the order of 10^{-6} m s⁻². Relatively larger residuals are mainly confined to regions characterized by strong currents and energetic mesoscale variability, including western boundary current extensions and parts of the Southern Ocean. Despite these localized enhancements, the overall balance index Bal remains below 5%, indicating that the reconstructed surface circulation satisfies the surface momentum balance to a high degree across the global ocean. The Fig.2 (d) illustrates the temporal evolution of the globally averaged Bal from 1993 to 2023. The global mean value remains stable over the entire period, with the global mean \pm standard deviation range varies between 1%~1.5%. No systematic drift or long-term trend is evident, demonstrating that the correction maintains a consistent level of dynamical balance throughout the multi-decadal record. Together, these results confirm that the AC-PIDNN correction yields a surface circulation that is dynamically self-consistent and temporally robust. For further validation, we compared the monthly observed data at the equatorial site (9°N, 140°W) (downloaded from <https://www.pmel.noaa.gov/tao/drupal/disdell/>) with the model results, as shown in Fig.2 (e-f). The comparison shows that the median errors between the corrected total flow field, geostrophic current, and Ekman-corrected current and the observed flow field are 0.072 m/s, 0.1996 m/s, and 0.1048 m/s, respectively, further demonstrating the accuracy of the model used in this study.

215
220
225

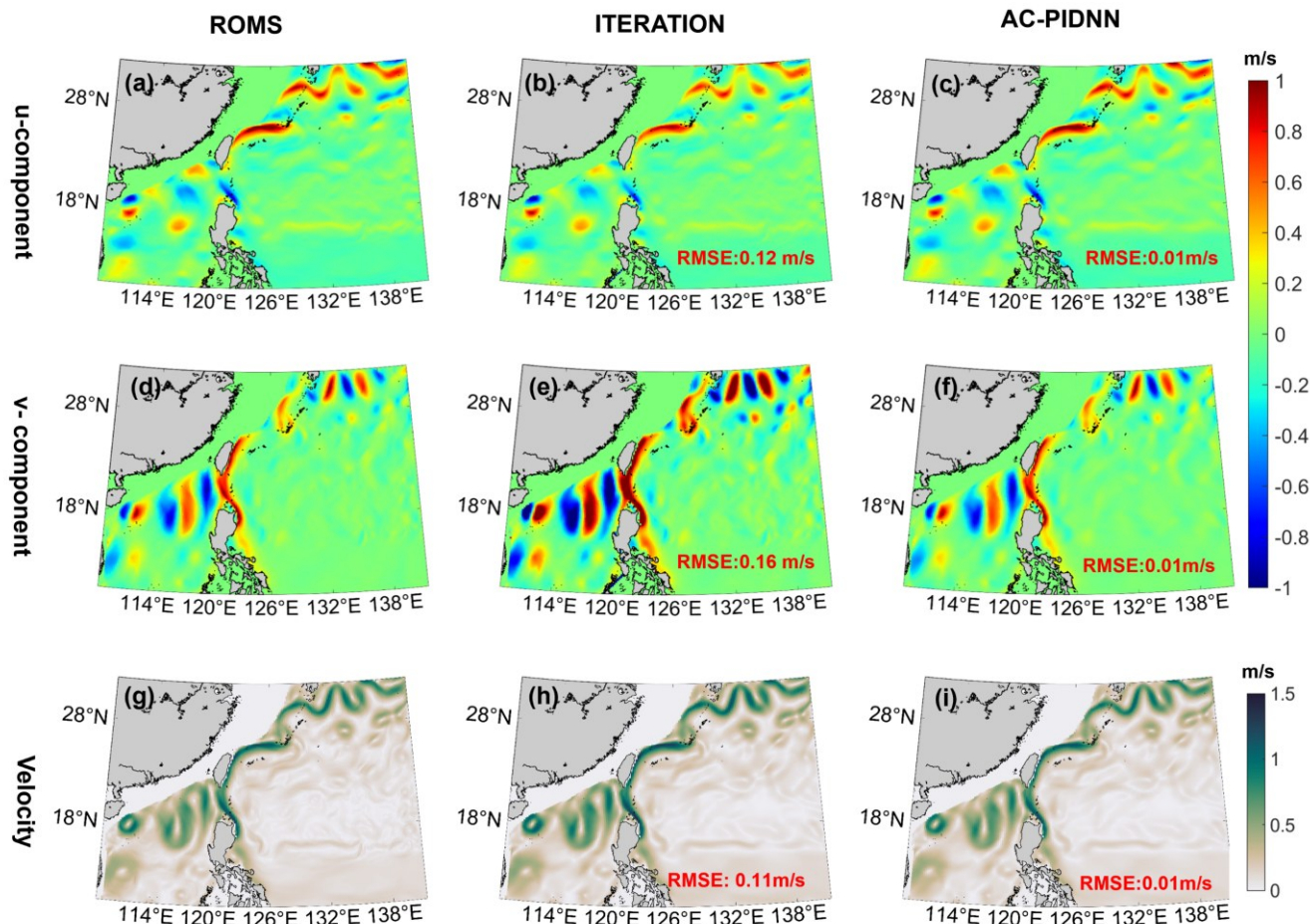


230 **Figure 2: Balance analysis of the corrected 30-year mean flow field within the momentum equations (4) and (5). Panel (a) 30-year**
mean residual of the zonal momentum equation, Bal_x ($m s^{-2}$), from 1993 to 2023; Panel (b) 30-year mean residual of the meridional
momentum equation, Bal_y , from 1993 to 2023; Panel (c) 30-year mean ratio of the magnitude of the momentum equation residuals
to the pressure gradient force, Bal , from 1993 to 2023. Panel (d) Time evolution of the globally averaged Bal from 1993 to 2023, with
the shaded area representing the ± 1 standard deviation range. Panel (e) comparison of monthly mean surface velocity at an
equatorial TAO mooring site ($9^{\circ}N$, $140^{\circ}W$) between observations and reconstructed currents (total current, geostrophic current,
and Ekman-corrected current). Panel (f) distribution of errors relative to the mooring observations for the total current, geostrophic
current, and Ekman-corrected current (boxplots show median and interquartile range; whiskers denote the non-outlier range).

240 To further evaluate the reconstruction accuracy, we conducted an additional validation using a high-resolution ROMS simulation as an independent reference (Fig. 3). In this experiment, the ROMS-simulated sea surface height was used as the



sole input to reconstruct the surface velocity field, ensuring a fair comparison between the baseline iterative method and the AC-PIDNN approach. As the ROMS simulation used herein neglects the Ekman component, this component is not taken into account in the present study. Figure 3 compares the reconstructed surface velocity fields with the ROMS reference in the northwestern Pacific Ocean. The zonal (u) and meridional (v) velocity components, as well as the velocity magnitude, are shown for the ROMS simulation, the Iteration method, and the AC-PIDNN reconstruction. The Iteration method reproduces the general structure of the velocity fields but exhibits substantial amplitude mismatches, particularly in regions of strong currents and mesoscale activity, with RMSE values of 0.12 m s^{-1} for u and 0.16 m s^{-1} for v , and 0.11 m s^{-1} for the magnitude of the velocity over the mapped domain. In contrast, the AC-PIDNN reconstruction reproduces the dominant spatial structures of the surface circulation more faithfully. The pathway and intensity of the western boundary current, as well as the surrounding mesoscale features, are captured with improved spatial coherence. Correspondingly, the RMSE is reduced to approximately 0.01 m s^{-1} for both velocity components and for the velocity magnitude, representing nearly an order-of-magnitude improvement over the iterative approach. Together with the momentum-balance diagnostics, the ROMS-based validation confirms that the corrected surface circulation is both dynamically consistent and quantitatively accurate under controlled conditions.



260 **Figure 3: Sea Surface Flow Field after Correction of Sea Surface Height Anomalies in the Northwestern Pacific using Iterative Method and AC-PIDNN. The first column shows the u-component, v-component, and flow field of the simulated data; the second column and column show the results corrected by the iterative method and AC-PIDNN method.**

4.2 Characteristics of the corrected surface circulation

In this section, we decompose the daily surface circulation (1993–2023) into geostrophic (\vec{V}_{geo}), Ekman (\vec{V}_{Ekman}), nonlinear advective (\vec{V}_{adv}) components. The detailed results for the Kuroshio region and the equatorial Pacific region are shown in Fig.S1 and S2, respectively. For each component, we analysed the zonal and meridional velocity components (u and v) together with the flow speed (Fig. 4).
 265

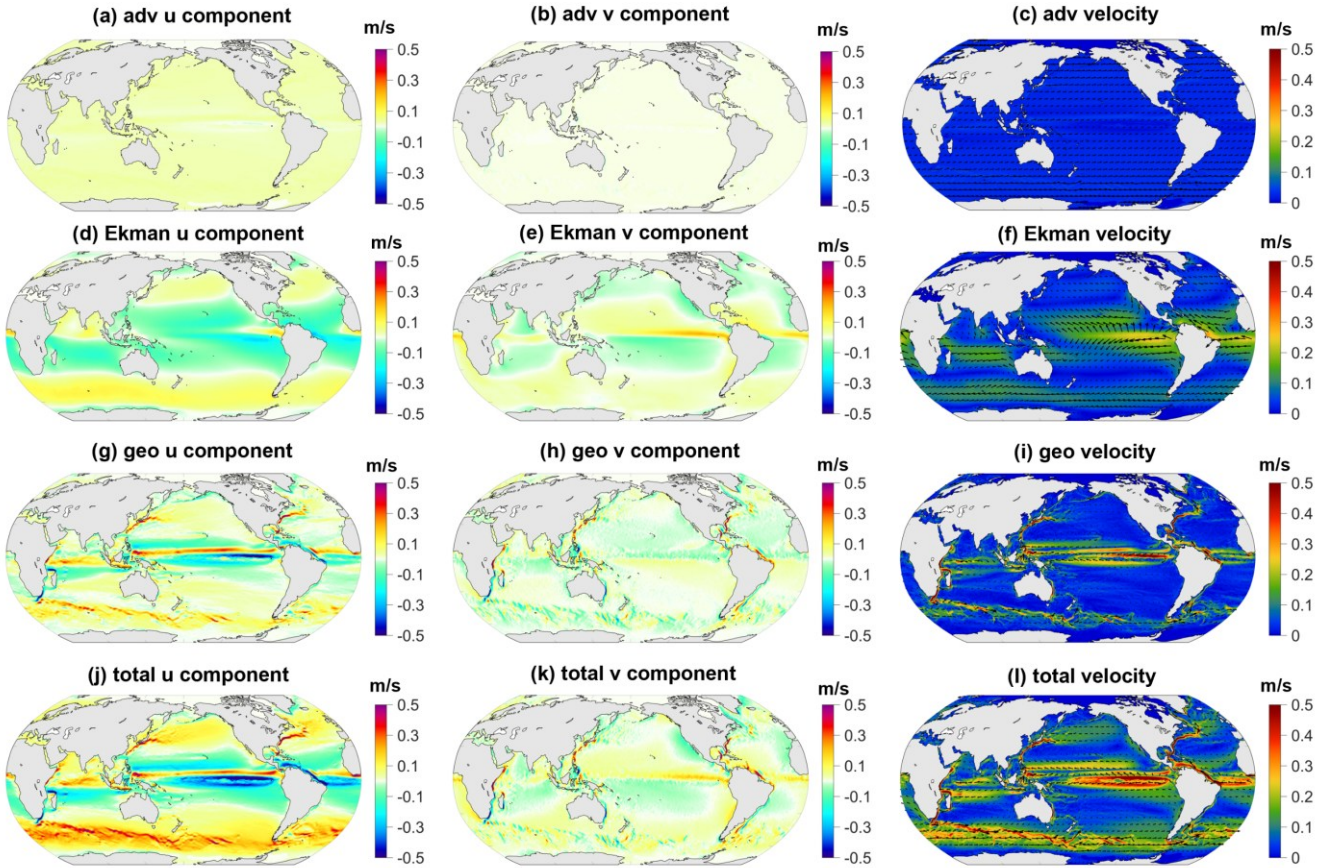
The nonlinear advective component (Fig.4 (a–c)) exhibits a relatively smaller magnitude. Both its zonal and meridional contributions are generally on the order of 10^{-2} m s^{-1} , with elevated values confined to dynamically active regions. These localized enhancements are most evident along the equatorial band, within western boundary current systems and their



270 extensions, and over parts of the Southern Ocean (Qiu et al., 2014). Over the majority of the open ocean, the advective component remains weak, indicating that its contribution to the corrected surface circulation is primarily expressed through regional and localized modulation rather than basin-scale influence. The Ekman component (Fig.4 (d–f)) displays a clear large-scale organization. Its zonal and meridional velocities show pronounced latitudinal banding over wide areas of the tropics and subtropics, consistent with the distribution of large-scale wind forcing. Typical Ekman velocities reach $O(10^{-1})$ m s⁻¹ in low- and mid-latitude regions, with reduced magnitudes toward higher latitudes.

275 The large-scale structure and intensity of the surface circulation are primarily controlled by the geostrophic flow (Fig.4 (g–i)). Both zonal and meridional geostrophic velocities exhibit strong signals associated with major current systems, including western boundary currents and their extensions and the Antarctic Circumpolar Current. The geostrophic speed commonly reaches $O(10^{-1} - 10^0)$ m s⁻¹. The weaker values are found in the interiors of subtropical gyres. As a result of the combined contributions, the total surface velocity field (Fig.4 (j–l)) closely resembles the geostrophic circulation in its overall structure, 280 while exhibiting systematic modifications in both magnitude and spatial details. In particular, westward zonal flow near the equator and Southern Ocean, and meridional transport in adjacent regions are strengthened relative to a purely geostrophic approximation, highlighting the cumulative influence of Ekman and nonlinear advective processes in shaping the corrected surface circulation. Neglecting these ageostrophic components would therefore bias the spatial distribution and magnitude of reconstructed surface currents.

285 Because the total velocity is defined as the linear sum of the three components, this decomposition provides a natural basis for examining their respective contributions to commonly used kinematic and energetic diagnostics, as discussed in the following section.



290 **Figure 4: Results of Sea Surface Circulation Correction from 1993 to 2023, using the AC-PIDNN model, incorporating geostrophic, nonlinear advective and Ekman components. Panels (a)–(c) show the u-component, v-component, and flow field of the nonlinear advective component; Panels (d)–(f) show the u-component, v-component, and flow field of the Ekman component; Panels (g)–(i) show the u-component, v-component, and flow field of the geostrophic component; Panels (j)–(l) show the u-component, v-component, and flow field of the total circulation.**

4.3 Impacts on kinematic and energetic diagnostics

295 This section examines the impacts of the velocity correction on commonly used kinematic and energetic diagnostics, including surface relative vorticity (VOR), divergence (DIV), and eddy kinetic energy (EKE). These variables are widely applied in studies of upper-ocean dynamics (Wunsch, 2025) and therefore provide an important perspective on the implications of the corrected surface circulation.

$$VOR = \frac{\partial v}{\partial x} - \frac{\partial u}{\partial y} \quad (19)$$



$$DIV = \frac{\partial u}{\partial x} + \frac{\partial v}{\partial y} \quad (20)$$

$$EKE = \frac{1}{2}(u'^2 + v'^2) \quad (21)$$

4.3.1 Vorticity

Sea surface relative vorticity is a key dynamical parameter that describes the rotational characteristics of the upper ocean flow, directly linked to flow shear, vortex structures, and angular momentum distribution (Zhang et al., 2024; Kwak and Richmond, 2014). The geostrophic component (Fig.5 (c)) dominates the large-scale structure of the relative vorticity field. Regions of strong positive and negative vorticity are closely aligned with major current systems, including western boundary currents, their downstream extensions, and the Antarctic Circumpolar Current. This distribution outlines the primary rotational framework of the surface circulation and reflects the strong shear associated with geostrophic jets and frontal zones. In addition to the geostrophic component, the wind-driven Ekman flow contributes significantly to the sea surface relative vorticity. Here, the Ekman component refers specifically to the vorticity generated by the velocity field that balances the wind stress forcing in the horizontal momentum equations (i.e., the Ekman flow), as distinct from the vertical Ekman pumping velocity associated with wind stress curl (Chen et al., 2020). While generally weaker in magnitude than geostrophic vorticity, this component exhibits distinct regional signatures. Enhanced Ekman vorticity (Fig.5 (b)) is particularly evident in tropical and subtropical basins where winds are strong and relatively steady, such as the trade wind belts and prevailing westerlies, where lateral shear in the Ekman velocity can generate significant vorticity signals (Chen et al., 2020). For instance, in equatorial regions, zonal wind stress can excite pronounced Ekman vorticity anomalies due to the variation of the Coriolis parameter. In contrast, the nonlinear vorticity (Fig.5 (a)) term arising from advection by the flow itself is typically about two orders of magnitude smaller in strength than the geostrophic and Ekman components. However, in regions of intense currents and strong shear, such as the Kuroshio Extension and Gulf Stream separation zones, nonlinear processes become crucial in modulating vorticity variability, energy cascade, and submesoscale vortex activities, and thus cannot be neglected (Chen et al., 2020). We present the 30-year average vorticity for the western boundary Kuroshio region and the wind-forced equatorial Pacific current region in Supplementary Fig.S3 (a-d) and Fig.S4 (a-d), respectively. This indicates that while the foundational structure of the large-scale vorticity field is set by geostrophic balance, with wind forcing and nonlinear dynamics providing an additional contribution to vorticity magnitude particularly in dynamically active regions.

4.3.2 Divergence

Sea surface horizontal divergence is a key physical quantity characterizing the divergent/convergent nature of the upper-ocean flow, with important implications for mass transport (Dubois et al., 2016). Unlike the vorticity field, the dynamical components of the divergence field exhibit distinct and contrasting contributions. From a dynamical decomposition perspective, the horizontal divergence of the geostrophic component (Fig.5 (g)) is negligible at the sea surface under the continuum layer



approximation, dictated by its non-divergent nature. Thus, the geostrophic flow contributes insignificantly to the large-scale sea surface horizontal divergence. In contrast, the nonlinear advective component (Fig.5 (e)) dominates the large-scale spatial pattern of the divergence field. Its magnitude is substantially larger than other components, forming prominent bands of divergence/convergence in regions of strong currents (e.g., western boundary current extensions) and vigorous eddy activity.

335 It is noteworthy that although the local amplitude of the advective divergence is large, its net contribution to basin-scale or global integrated divergence is modest due to the cancellation between extensive positive and negative regions. The Ekman component of divergence (Fig.5 (f)), however, originates directly from Ekman pumping/suction driven by wind stress curl. Its local intensity is typically weaker than the advective component. Due to its more spatially coherent sign (e.g., divergence over regions of positive wind stress curl and convergence over negative curl regions), the Ekman component contributes

340 significantly to the domain-averaged or net divergent effect at regional or global scales, and its magnitude is non-negligible. For instance, in the major wind belts (trade winds, westerlies), Ekman divergence forms a key driver for large-scale vertical circulation cells, such as the subtropical gyres (Roquet et al., 2025). To further illustrate the impacts of nonlinear processes and wind forcing on sea surface divergence, we present the 30-year average vorticity for the western boundary Kuroshio region and the wind-forced equatorial Pacific current region in Supplementary Fig.S3 (e-h) and Fig.S4 (e-h), respectively.

345 4.3.3 Eddy Kinetic Energy

Eddy Kinetic Energy is an integrated metric for the intensity of mesoscale variability, representing the perturbation energy of the flow velocity field relative to its temporal mean. It serves as a key parameter for assessing the energetic consistency and dynamical plausibility of the corrected velocity field (Huo et al., 2024). As shown in Fig.5 (i-l) the global EKE distribution derived from the corrected circulation field, which incorporates geostrophic, Ekman, and nonlinear advective components

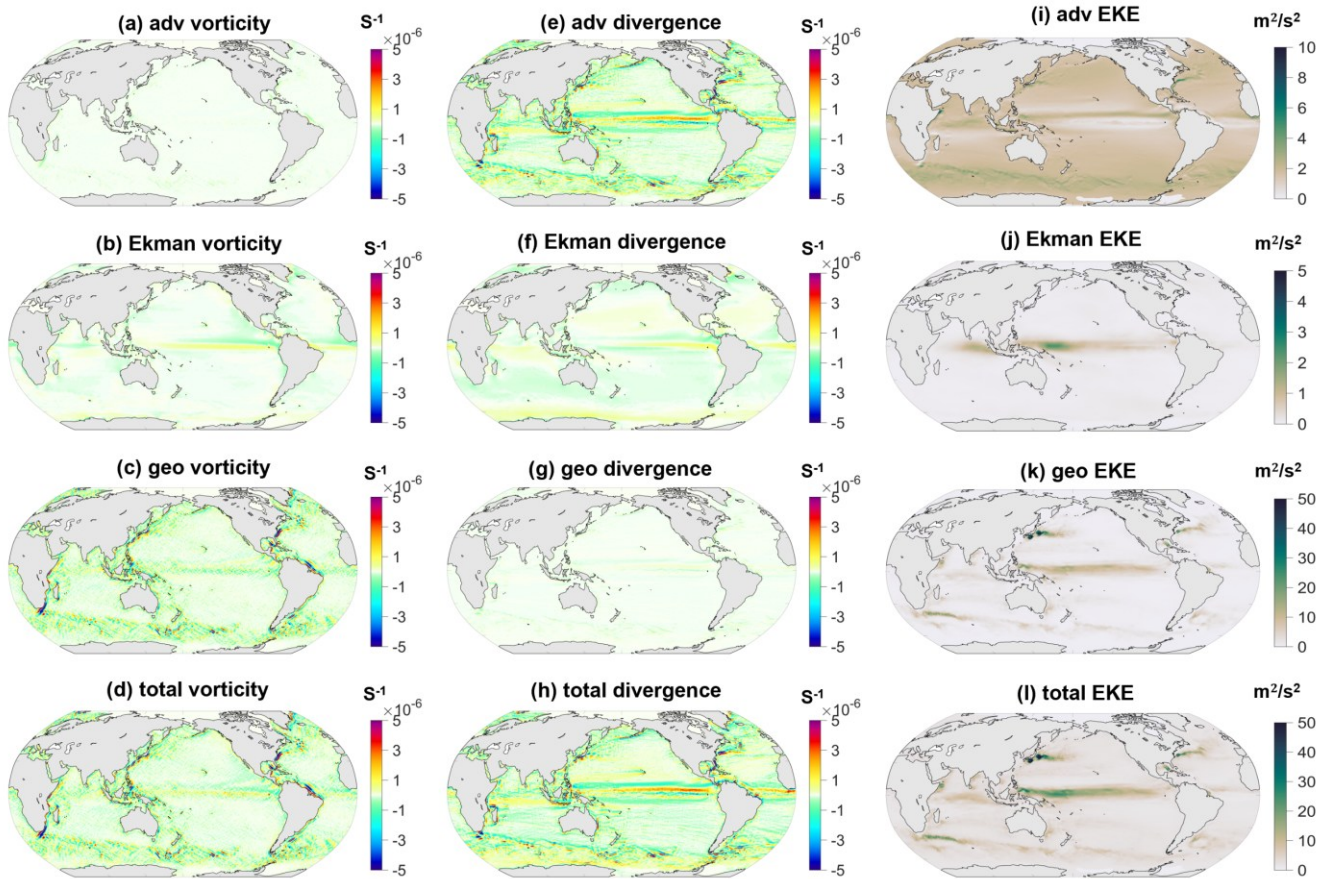
350 exhibits the well-documented pattern of high-energy regimes: primarily concentrated in western boundary current extensions (e.g., the Kuroshio Extension, Gulf Stream Extension), the core regions of the Antarctic Circumpolar Current, and equatorial current systems, all areas of high dynamical activity (Su et al., 2023). To further illustrate this point, Supplementary Fig.S3 (i-l) and Fig.S4 (i-l) present the 30-year mean EKE characteristics in the equatorial Pacific region and the Kuroshio region, respectively. These energetic hotspots are closely linked to strong shear, instability processes, and active mesoscale eddy

355 generation. Compared to EKE estimates based solely on the geostrophic approximation, the inclusion of the Ekman and nonlinear advective components does not introduce spurious amplification of the total kinetic energy. Instead, it redistributes the energy spatially in a physically consistent manner. The correction primarily modulates the structure of the EKE field rather than significantly altering its global intensity magnitude. Specifically, in regions where wind forcing is pronounced, such as the equatorial and subtropical zones, incorporating the Ekman component provides a more realistic representation of

360 fluctuating energy directly generated by wind variability. Meanwhile, in the vicinity of strong current edges and frontal zones, nonlinear advective processes dominate in shaping the fine-scale structure of EKE, such as energy cascade and eddy-mean flow interactions (Adeagbo et al., 2022). In summary, the multi-component velocity correction scheme redistributes the spatial pattern of EKE in a manner consistent with physical mechanisms while preserving the overall energetic framework of the



365 surface circulation. This enhances the capability of the EKE field to characterize mesoscale processes, energy transfer pathways, and mixing efficiency, yielding a representation that is closer to the true dynamical context of the ocean.



370 **Figure 5: 30-year average global sea surface dynamic parameter characteristics. Panels (a)–(d) showing the vorticity of the advective, Ekman, geostrophic, and total components, respectively; Panels (e)–(h) showing the divergence of the advective, Ekman, geostrophic, and total components, respectively; Panels (i)–(l) showing the eddy kinetic energy (EKE) of the advective, Ekman, geostrophic, and total components, respectively.**

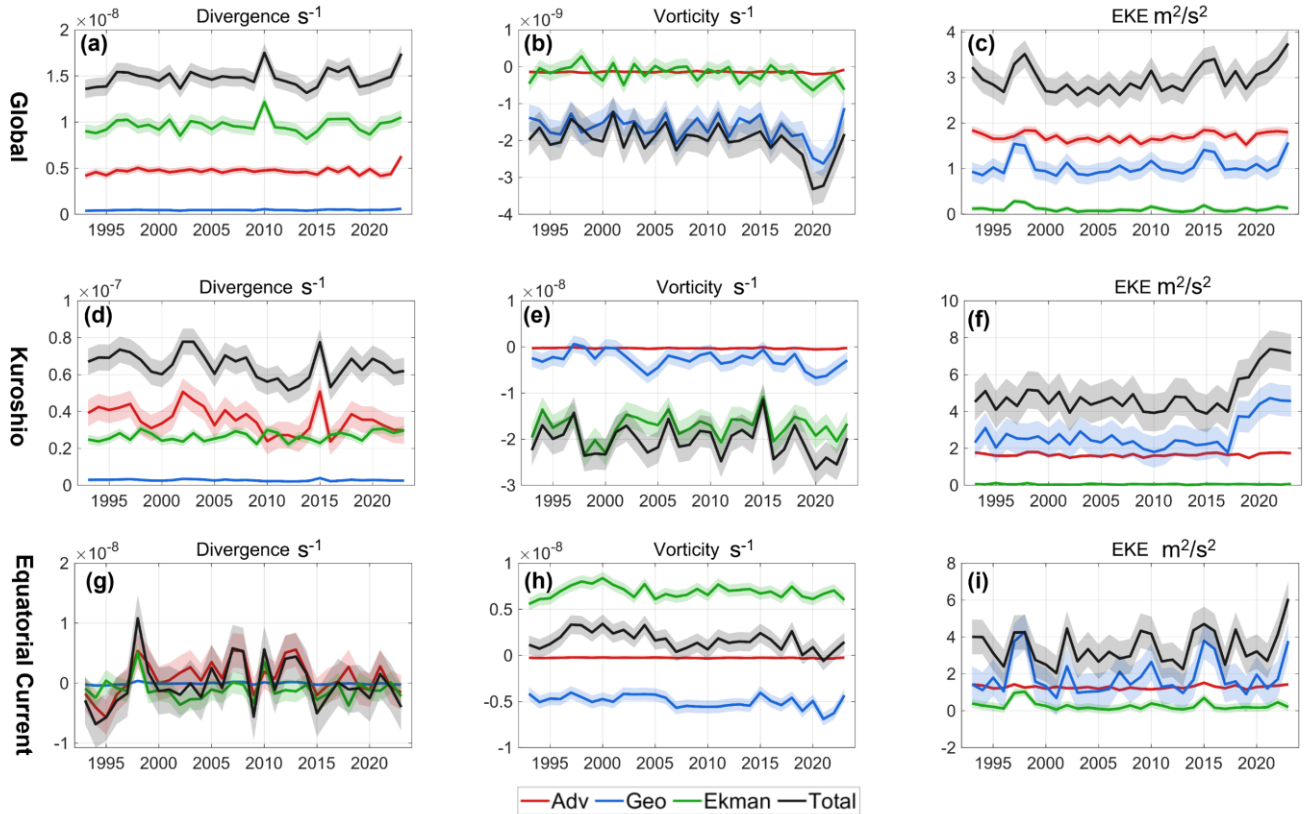
4.3.4 Temporal Evolution of Dynamical Diagnostics

To analyze the long-term variations in the three dynamic parameters mentioned above, Fig.6 presents the 30-year time series for the global ocean, the Kuroshio region (110°E–175°E, 12°N–50°N), and the Equatorial Current region (60°W–110°E, 20°S–20°N). On a global scale (Fig.6 (a-c)), the interannual variability of total divergence ($\mathcal{O}(10^{-8}) \text{ s}^{-1}$) is primarily dominated by the Ekman component ($\mathcal{O}(10^{-9}) \text{ s}^{-1}$), with the nonlinear component ($\mathcal{O}(10^{-9}) \text{ s}^{-1}$) also contributing significantly, and their variation trends are largely consistent. The magnitude of variability in nonlinear divergence is smaller than that of the Ekman



380 component but significantly larger than the negligible geostrophic divergence ($\mathcal{O}(10^{-10}) \text{ s}^{-1}$). The total relative vorticity field ($\mathcal{O}(10^{-9}) \text{ s}^{-1}$) is mainly determined by the combined effects of the geostrophic component ($\mathcal{O}(10^{-9}) \text{ s}^{-1}$) and the Ekman component ($\mathcal{O}(10^{-10}) \text{ s}^{-1}$). In terms of trends, the Ekman vorticity exhibits a weakening trend, whereas both geostrophic and total vorticities show a long-term enhancement of negative vorticity. No significant interannual signal is detected in nonlinear vorticity. Regarding eddy kinetic energy (EKE), the trend in total EKE aligns with that of geostrophic EKE but is notably modulated by nonlinear processes. Moreover, the magnitudes of the nonlinear and geostrophic components are comparable, with the nonlinear EKE being higher in most years, yet both remain within the same order of magnitude ($\mathcal{O}(10^0\text{--}10^1) \text{ m}^2 \text{ s}^{-2}$).

385 On a regional scale, two representative areas, the Kuroshio region and the Equatorial Current region are selected for analysis (Fig.6 (d-i)). In the Kuroshio region, the variation in total divergence follows the trend of the nonlinear component, although the contribution of the Ekman component is non-negligible, particularly in equatorial areas. The magnitude of divergence in the Kuroshio region ($\mathcal{O}(10^{-8}) \text{ s}^{-1}$) is larger than that in the Equatorial Current region ($\mathcal{O}(10^{-9}) \text{ s}^{-1}$). Regarding vorticity, the Kuroshio region is dominated by negative vorticity, with the absolute value of the Ekman component being significantly larger than that of the geostrophic component. In contrast, the Equatorial Current region exhibits positive Ekman vorticity and negative geostrophic vorticity, with total vorticity primarily contributed by the Ekman component. Additionally, 390 the magnitudes of geostrophic and total vorticities in the Kuroshio region ($\mathcal{O}(10^{-8}) \text{ s}^{-1}$) exceed those in the Equatorial Current region ($\mathcal{O}(10^{-9}) \text{ s}^{-1}$). For EKE, variations in both regions are mainly governed by the geostrophic component. The trend in total EKE in the Equatorial Current region closely resembles that of its geostrophic component, whereas the Kuroshio region has shown an increasing trend in EKE since approximately 2017. In terms of magnitude, total EKE, geostrophic EKE, and 395 nonlinear EKE are all on the order of $\mathcal{O}(10^0\text{--}10^1) \text{ m}^2 \text{ s}^{-2}$. The Ekman EKE in the Equatorial Current region ($\mathcal{O}(10^{-1}) \text{ m}^2 \text{ s}^{-2}$) is larger than that in the Kuroshio region ($\mathcal{O}(10^{-2}) \text{ m}^2 \text{ s}^{-2}$).



400 **Figure 6: The annual mean variations in sea surface divergence, vorticity, and EKE from 1993 to 2023 for the global ocean, the Kuroshio region, and the equatorial current region. Panels (a)–(c) illustrate the interannual changes in globally averaged sea surface divergence, vorticity, and EKE; Panels (d)–(f) show the corresponding variations in the Kuroshio region (110°–175°E, 12°–50°N); and panels (g)–(i) display the changes in the equatorial current region (60°W–110°E, 20°S–20°N). The shaded area around each curve represents the ± 1 standard deviation range.**

405 **5 Code and data availability**

The code for AC-PIDNN is available at <https://github.com/cgxcgxcgxcg/AC-PIDNN>. The global sea surface circulation dataset corrected for the period 1993–2023 in this study can be accessed via <https://doi.org/10.5281/zenodo.19966715> (Cui and Cai, 2026). This dataset has a spatial resolution of 0.25°, and each daily flow field file contains the variable names and their descriptions as listed in Table 1. Furthermore, the table outlines the Dataset ID corresponding to the satellite data product (global gridded geostrophic currents and surface Ekman currents) obtained from the Copernicus Marine Service at: <https://data.marine.copernicus.eu/product>.



Table 1 Dataset Variable Information

Values	size	definition	Dataset ID
sla	720×1440	Sea Level Anomaly, sourced from the AVISO dataset.	cmems_obs-
ugeo	720×1440	Zonal (u) component of the geostrophic current, sourced from the AVISO dataset.	sl_glo_phy-ssh_my_allsat-l4-
vgeo	720×1440	Meridional (v) component of the geostrophic current, sourced from the AVISO dataset.	duacs-0.125deg_PID
uekman	720×1440	Zonal (u) component of the surface (0 m) Ekman current, sourced from the global Copernicus Ocean (GLOBCURRENT) surface and 15-meter Ekman and geostrophic current datasets.	cmems_obs-mob_glo_phy-cur_my_0.25deg_PID-
vekman	720×1440	Meridional (v) component of the surface (0 m) Ekman current, sourced from the global Copernicus Ocean (GLOBCURRENT) surface and 15-meter Ekman and geostrophic current datasets.	m
uadv	720×1440	Zonal (u) component of the nonlinear advective term.	-
vadv	720×1440	Meridional (v) component of the nonlinear advective term.	-
utotal	720×1440	Zonal (u) component of the total flow field corrected by the AC-PIDNN model.	-
vtotal	720×1440	Meridional (v) component of the total flow field corrected by the AC-PIDNN model.	-
resu	720×1440	Residual of the zonal (u) momentum (Navier-Stokes) equation.	-
Resu			
resv	720×1440	Residual of the meridional (v) momentum (Navier-Stokes) equation.	-
Resv			
lon	1 × 1440	Longitude coordinates, ranging from -179.75°E to 180°E with a 0.25° resolution.	-
lat	720×1	Latitude coordinates, ranging from -89.75°N to 90°N with a 0.25° resolution.	-

6 Conclusions

415 A key contribution of this study is the development of a physics-informed deep learning framework to correct sea surface currents and quantify their dynamical components. By explicitly incorporating physical constraints, the framework substantially improves the dynamical consistency of reconstructed surface circulation and yields a global daily dataset for



1993-2023. Our results show that, although ageostrophic components are generally smaller than the geostrophic flow, they make important contributions to the total surface circulation, especially in energetic regions such as western boundary currents and the Kuroshio Extension. On a global scale, the mean velocity of the total flow field is on the order of $O(10^{-2}-10^{-1})$ m s⁻¹, with the Ekman, geostrophic, and nonlinear components each exhibiting magnitudes of $O(10^{-2})$ m s⁻¹. In particular, nonlinear contributions have limited influence on relative vorticity, as the dominant rotational structure is captured by the geostrophic circulation. In contrast, the nonlinear corrections strongly affect surface divergence and eddy kinetic energy, revealing aspects of ocean surface dynamics that are not captured by geostrophic circulation alone. These findings show that resolving ageostrophic dynamics is essential for a more complete understanding of global surface circulation and its variability.

Author contribution:

Guangxi Cui: Formal analysis, Investigation, Methodology, Writing (original draft preparation); **Ka-Veng Yuen:** Methodology, Conceptualization, Writing (review and editing); **Ying Chen:** Investigation, Writing (review and editing); **Zhiqiang Liu:** Methodology, Writing (review and editing); **Dingqi Yang:** Methodology, Writing (review and editing); **Guanglinag Liu:** Resources, Writing (review and editing); **Zhongya Cai:** Methodology, Conceptualization, Supervision, Writing (review and editing)

Competing interests:

The authors declare that they have no conflict of interest

Acknowledgement

This work was funded by the National Natural Science Foundation of China (42376024, 42450181), Science and Technology Development Fund, Macau SAR (File/Project no. 0093/2020/A2, 001/2024/SKL); This work is supported by Centre for Regional Oceans in University of Macau (SP2025-00005-CRO); This work is supported by CORE, which is a joint research center for ocean research between Laoshan Laboratory and HKUST, and substantially supported by a grant from the Research Grants Council of the Hong Kong Special Administrative Region, China (Project Reference Number: AoE/P-601/23-N). The simulation was performed at the SICC, which is supported by the SKL-IOTSC, University of Macau.

References

Adeagbo, O. S., Du, Y., Wang, T., and Wang, M.: Eddy–mean flow interactions in the Agulhas leakage region, *Journal of Oceanography*, 78, 151-161, 10.1007/s10872-022-00637-6, 2022.
Aluie, H., Hecht, M., and Vallis, G. K.: Mapping the Energy Cascade in the North Atlantic Ocean: The Coarse-Graining Approach, *Journal of Physical Oceanography*, 48, 225-244, <https://doi.org/10.1175/JPO-D-17-0100.1>, 2018.



- Andres, M., Park, J.-H., Wimbush, M., Zhu, X.-H., Chang, K.-I., and Ichikawa, H.: Study of the Kuroshio/Ryukyu Current system based on satellite-altimeter and in situ measurements, *Journal of Oceanography*, 64, 937-950, <https://doi.org/10.1007/s10872-008-0077-2>, 2008.
- 450 Armitage, T. W. K., Bacon, S., Ridout, A. L., Petty, A. A., Wolbach, S., and Tsamados, M.: Arctic Ocean surface geostrophic circulation 2003–2014, *The Cryosphere*, 11, 1767-1780, <https://doi.org/10.5194/tc-11-1767-2017>, 2017.
- Arnason, G., Haltiner, G., and Frawley, M.: Higher-order geostrophic wind approximations, *Monthly Weather Review*, 90, 175-185, [https://doi.org/10.1175/1520-0493\(1962\)090<0175:HGWA>2.0.CO;2](https://doi.org/10.1175/1520-0493(1962)090<0175:HGWA>2.0.CO;2), 1962.
- Bonino, G., Galimberti, G., Masina, S., McAdam, R., and Clementi, E.: Machine learning methods to predict sea surface temperature and marine heatwave occurrence: a case study of the Mediterranean Sea, *Ocean Sci.*, 20, 417-432, <https://doi.org/10.5194/os-20-417-2024>, 2024.
- 455 Buckingham, C. E., Gula, J., and Carton, X.: The Role of Curvature in Modifying Frontal Instabilities. Part I: Review of Theory and Presentation of a Nondimensional Instability Criterion, *Journal of Physical Oceanography*, 51, 299-315, <https://doi.org/10.1175/JPO-D-19-0265.1>, 2021.
- Cao, Y., Dong, C., Qiu, Z., Bethel, B. J., Shi, H., Lü, H., and Cheng, Y.: Corrections of Mesoscale Eddies and Kuroshio Extension Surface Velocities Derived from Satellite Altimeters, *Remote Sensing*, 15, <https://doi.org/10.3390/rs15010184>, 2023a.
- Cao, Y., Dong, C., Stegner, A., Bethel, B. J., Li, C., Dong, J., Lü, H., and Yang, J.: Global Sea Surface Cyclogeostrophic Currents Derived From Satellite Altimetry Data, *Journal of Geophysical Research: Oceans*, 128, e2022JC019357, <https://doi.org/10.1029/2022JC019357>, 2023b.
- 465 Chen, K., Gaube, P., and Pallàs-Sanz, E.: On the Vertical Velocity and Nutrient Delivery in Warm Core Rings, *Journal of Physical Oceanography*, 50, 1557-1582, <https://doi.org/10.1175/JPO-D-19-0239.1>, 2020.
- Cho, S. W., Choi, J. G., Kim, D., Lu, W., and Jo, Y. H.: Deriving hourly diagnostic surface velocity fields considering inertia and an application in the Yellow Sea, *EGU sphere*, 2025, 1-24, <https://doi.org/10.5194/egusphere-2025-2748>, 2025.
- Cui, G., Yuen, K.-V., Cai, Z., Liu, Z., and Zhang, G.: Research on adaptive ocean remote sensing target detection framework: An efficient solution based on the broad learning system, *ISPRS Journal of Photogrammetry and Remote Sensing*, 229, 188-210, <https://doi.org/10.1016/j.isprsjprs.2025.08.020>, 2025.
- Dong, C., Xu, G., Han, G., Bethel, B. J., Xie, W., and Zhou, S.: Recent Developments in Artificial Intelligence in Oceanography, *Ocean-Land-Atmosphere Research*, 2022, <https://doi.org/10.34133/2022/9870950>, 2022.
- Douglass, E. M. and Richman, J. G.: Analysis of ageostrophy in strong surface eddies in the Atlantic Ocean, *Journal of Geophysical Research: Oceans*, 120, 1490-1507, <https://doi.org/10.1002/2014JC010350>, 2015.
- 475 Cui, G., Cai, Z.: Daily Global Sea Surface Ageostrophic Current Dataset from 1993–2023 via Physics-Informed Deep Learning [Data set]. Zenodo, <https://doi.org/10.5281/zenodo.19966715>, 2026
- Du, Y., Dong, X., Jiang, X., Zhang, Y., Zhu, D., Sun, Q., Wang, Z., Niu, X., Chen, W., and Zhu, C.: Ocean surface current multiscale observation mission (OSCOM): Simultaneous measurement of ocean surface current, vector wind, and temperature, *Progress in Oceanography*, 193, 102531, <https://doi.org/10.1016/j.pocean.2021.102531>, 2021.
- 480 Dubois, M., Rossi, V., Ser-Giacomi, E., Arnaud-Haond, S., López, C., and Hernández-García, E.: Linking basin-scale connectivity, oceanography and population dynamics for the conservation and management of marine ecosystems, *Global Ecology and Biogeography*, 25, 503-515, <https://doi.org/10.1111/geb.12431>, 2016.
- Edwards, C. A., De Mey-Frémaux, P., Barceló-Llull, B., Charria, G., Choi, B.-J., Halliwell, G. R., Hole, L. R., Kerry, C., Kourafalou, V. H., Kurapov, A. L., Moore, A. M., Mourre, B., Oddo, P., Pascual, A., Roughan, M., Skandrani, C., Storto, A., Vervatis, V., and Wilkin, J. L.: Assessing impacts of observations on ocean circulation models with examples from coastal, shelf, and marginal seas, Volume 11 - 2024, <https://doi.org/10.3389/fmars.2024.1458036>, 2024.
- 485 Fan, S., Kudryavtsev, V., Yurovsky, Y., and Zhang, B.: Reconstructing ocean surface current vector field from SAR doppler shift measurements, *Remote Sensing of Environment*, 328, 114855, <https://doi.org/10.1016/j.rse.2025.114855>, 2025.
- 490 Fraser, N. J., Fox, A. D., Cunningham, S. A., Rath, W., Schwarzkopf, F. U., and Biastoch, A.: Vertical Velocity Dynamics in the North Atlantic and Implications for AMOC, *Journal of Physical Oceanography*, 54, 2011-2024, <https://doi.org/10.1175/JPO-D-23-0229.1>, 2024.
- Glorot, X. and Bengio, Y.: Understanding the difficulty of training deep feedforward neural networks, *JMLR Workshop and Conference Proceedings*, 9, 249-256, 2010.



- 495 Hiron, L., Nolan, D. S., and Shay, L. K.: Study of Ageostrophy during Strong, Nonlinear Eddy-Front Interaction in the Gulf of Mexico, *Journal of Physical Oceanography*, 51, 745-755, <https://doi.org/10.1175/JPO-D-20-0182.1>, 2021.
- Huo, J., Zhang, J., Yang, J., Li, C., Liu, G., and Cui, W.: High kinetic energy mesoscale eddy identification based on multi-task learning and multi-source data, *International Journal of Applied Earth Observation and Geoinformation*, 128, 103714, <https://doi.org/10.1016/j.jag.2024.103714>, 2024.
- 500 Ioannou, A., Stegner, A., Tuel, A., LeVu, B., Dumas, F., and Speich, S.: Cyclostrophic Corrections of AVISO/DUACS Surface Velocities and Its Application to Mesoscale Eddies in the Mediterranean Sea, *Journal of Geophysical Research: Oceans*, 124, 8913-8932, <https://doi.org/10.1029/2019JC015031>, 2019.
- Jang, E., Kim, Y. J., Im, J., Park, Y.-G., and Sung, T.: Global sea surface salinity via the synergistic use of SMAP satellite and HYCOM data based on machine learning, *Remote Sensing of Environment*, 273, 112980, <https://doi.org/10.1016/j.rse.2022.112980>, 2022.
- 505 Kafiabad, H. A., Savva, M. A. C., and Vanneste, J.: Diffusion of inertia-gravity waves by geostrophic turbulence, *Journal of Fluid Mechanics*, 869, R7, <https://doi.org/10.1017/jfm.2019.300>, 2019.
- Kartal, S.: Assessment of the spatiotemporal prediction capabilities of machine learning algorithms on Sea Surface Temperature data: A comprehensive study, *Engineering Applications of Artificial Intelligence*, 118, 105675, <https://doi.org/10.1016/j.engappai.2022.105675>, 2023.
- 510 Kingma, D. P. and Ba, J. J. C.: Adam: A Method for Stochastic Optimization, abs/1412.6980, 2014.
- Kumar, C., Podestá, G., Kilpatrick, K., and Minnett, P.: A machine learning approach to estimating the error in satellite sea surface temperature retrievals, *Remote Sensing of Environment*, 255, 112227, <https://doi.org/10.1016/j.rse.2020.112227>, 2021.
- Kwak, Y. S. and Richmond, A. D.: Dependence of the high-latitude lower thermospheric wind vertical vorticity and horizontal divergence on the interplanetary magnetic field, *Journal of Geophysical Research: Space Physics*, 119, 1356-1368, <https://doi.org/10.1002/2013JA019589>, 2014.
- 515 Lenain, L., Srinivasan, K., Barkan, R., and Pizzo, N.: An unprecedented view of ocean currents from geostationary satellites, *Nature Geoscience*, 10.1038/s41561-026-01943-0, 2026.
- Li, X., Liu, B., Zheng, G., Ren, Y., Zhang, S., Liu, Y., Gao, L., Liu, Y., Zhang, B., and Wang, F.: Deep-learning-based information mining from ocean remote-sensing imagery, *National Science Review*, 7, 1584-1605, <https://doi.org/10.1093/nsr/nwaa047>, 2020.
- 520 Li, Z., Cai, Z., Liu, Z., Wang, X., and Hu, J.: A novel identification method for unrevealed mesoscale eddies with transient and weak features-Capricorn Eddies as an example, *Remote Sensing of Environment*, 274, 112981, <https://doi.org/10.1016/j.rse.2022.112981>, 2022.
- 525 Liu, Y., He, Q., Zhan, W., Guo, M., Zheng, Y., Shen, X., and Zhan, H.: Heterogeneity of phytoplankton response to submesoscale processes in the global ocean, *Communications Earth & Environment*, 6, 386, <https://doi.org/10.1038/s43247-025-02365-3>, 2025.
- Manucharyan, G. E., Siegelman, L., and Klein, P.: A Deep Learning Approach to Spatiotemporal Sea Surface Height Interpolation and Estimation of Deep Currents in Geostrophic Ocean Turbulence, *Journal of Advances in Modeling Earth Systems*, 13, e2019MS001965, <https://doi.org/10.1029/2019MS001965>, 2021.
- 530 Masuda, Y., Yamanaka, Y., Smith, S. L., Hirata, T., Nakano, H., Oka, A., and Sumata, H.: Photoacclimation by phytoplankton determines the distribution of global subsurface chlorophyll maxima in the ocean, *Communications Earth & Environment*, 2, 128, <https://doi.org/10.1038/s43247-021-00201-y>, 2021.
- Morales-Márquez, V., Hernández-Carrasco, I., Fox-Kemper, B., and Orfila, A.: Ageostrophic Contribution by the Wind and Waves Induced Flow to the Lateral Stirring in the Mediterranean Sea, *Journal of Geophysical Research: Oceans*, 128, e2022JC019135, <https://doi.org/10.1029/2022JC019135>, 2023.
- 535 Mulet, S., Rio, M. H., Etienne, H., Artana, C., Cancet, M., Dibarboure, G., Feng, H., Husson, R., Picot, N., Provost, C., and Strub, P. T.: The new CNES-CLS18 global mean dynamic topography, *Ocean Science*, 17, 789-808, <https://doi.org/10.5194/os-17-789-2021>, 2021.
- 540 Penven, P., Halo, I., Pous, S., and Marié, L.: Cyclogeostrophic balance in the Mozambique Channel, *Journal of Geophysical Research: Oceans*, 119, 1054-1067, <https://doi.org/10.1002/2013JC009528>, 2014.
- Qin, Y., Su, C., Chu, D., Zhang, J., and Song, J.: A review of application of machine learning in storm surge problems, *Journal of Marine Science Engineering*, 11, 1729, <https://doi.org/10.3390/jmse11091729>, 2023.



- 545 Qiu, B., Chen, S., Klein, P., Sasaki, H., and Sasai, Y.: Seasonal Mesoscale and Submesoscale Eddy Variability along the North Pacific Subtropical Countercurrent, *Journal of Physical Oceanography*, 44, 3079-3098, <https://doi.org/10.1175/JPO-D-14-0071.1>, 2014.
- Qiu, C., Mao, H., Wang, Y., Yu, J., Su, D., and Lian, S.: An irregularly shaped warm eddy observed by Chinese underwater gliders, *Journal of oceanography*, 75, 139-148, <https://doi.org/10.1007/s10872-018-0490-0>, 2019.
- 550 Rio, M.-H., Mulet, S., and Picot, N.: Beyond GOCE for the ocean circulation estimate: Synergetic use of altimetry, gravimetry, and in situ data provides new insight into geostrophic and Ekman currents, *Geophysical Research Letters*, 41, 8918-8925, <https://doi.org/10.1002/2014GL061773>, 2014.
- Roquet, F., Bell, M. J., de Boer, A. M., Ferreira, D., Jones, C. S., LaCasce, J. H., de Lavergne, C., Marshall, D. P., Munday, D. R., Nycander, J., and Ödalen, M.: Controls of the global overturning circulation of the ocean, *npj Climate and Atmospheric Science*, 8, 304, 10.1038/s41612-025-01185-8, 2025.
- 555 Ruiz, S., Pelegrí, J. L., Emelianov, M., Pascual, A., and Mason, E.: Geostrophic and ageostrophic circulation of a shallow anticyclonic eddy off Cape Bojador, *Journal of Geophysical Research: Oceans*, 119, 1257-1270, <https://doi.org/10.1002/2013JC009169>, 2014.
- Shang, J., Shi, H., Yuan, M., Wu, Q., Lv, A., Dou, F., Yin, H., Liu, L., and Hu, X.: Satellite-Ground Integrated External Calibration of the WindRAD Scatterometer Onboard FY-3E Satellite, *IEEE Transactions on Geoscience and Remote Sensing*, 63, 1-10, <https://doi.org/10.1109/TGRS.2025.3526834>, 2025.
- 560 Shankar, D., Vinayachandran, P. N., and Unnikrishnan, A. S.: The monsoon currents in the north Indian Ocean, *Progress in Oceanography*, 52, 63-120, [https://doi.org/10.1016/S0079-6611\(02\)00024-1](https://doi.org/10.1016/S0079-6611(02)00024-1), 2002.
- Shchepetkin, A. F. and McWilliams, J. C.: The regional oceanic modeling system (ROMS): a split-explicit, free-surface, topography-following-coordinate oceanic model, *Ocean Modelling*, 9, 347-404, <https://doi.org/10.1016/j.ocemod.2004.08.002>, 2005.
- 565 Sinha, A. and Abernathy, R.: Estimating Ocean Surface Currents With Machine Learning, *Frontiers in Marine Science*, 8, <https://doi.org/10.3389/fmars.2021.672477>, 2021.
- Srinivasan, M. and Tsontos, V.: Satellite Altimetry for Ocean and Coastal Applications: A Review, *Remote Sensing*, 15, <https://doi.org/10.3390/rs15163939>, 2023.
- 570 Su, F., Fan, R., Yan, F., Meadows, M., Lyne, V., Hu, P., Song, X., Zhang, T., Liu, Z., Zhou, C., Pei, T., Yang, X., Du, Y., Wei, Z., Wang, F., Qi, Y., and Chai, F.: Widespread global disparities between modelled and observed mid-depth ocean currents, *Nature Communications*, 14, 2089, 10.1038/s41467-023-37841-x, 2023.
- Su, H., Xie, W., You, L., Li, S., Lin, D., and Wang, A.: Detecting global ocean subsurface density change with high-resolution via dual-task densely-former, *ISPRS Journal of Photogrammetry and Remote Sensing*, 233, 158-179, <https://doi.org/10.1016/j.isprsjprs.2026.01.026>, 2026.
- 575 Sudre, J., Maes, C., and Garçon, V.: On the global estimates of geostrophic and Ekman surface currents, *Limnology Oceanography: Fluids Environments*, 3, 1-20, <https://doi.org/10.1215/21573689-2071927>, 2013.
- Thomas, J. and Daniel, D.: Forward flux and enhanced dissipation of geostrophic balanced energy, *Journal of Fluid Mechanics*, 911, A60, <https://doi.org/10.1017/jfm.2020.1026>, 2021.
- 580 Timmermans, M.-L. and Marshall, J.: Understanding Arctic Ocean Circulation: A Review of Ocean Dynamics in a Changing Climate, *Journal of Geophysical Research: Oceans*, 125, e2018JC014378, <https://doi.org/10.1029/2018JC014378>, 2020.
- Uchida, H. and Imawaki, S.: Eulerian mean surface velocity field derived by combining drifter and satellite altimeter data, *Geophys. Res. Lett.*, 30, <https://doi.org/10.1029/2002GL016445>, 2003.
- 585 Ueno, H., Bracco, A., Barth, J. A., Budyansky, M. V., Hasegawa, D., Itoh, S., Kim, S. Y., Ladd, C., Lin, X., Park, Y.-G., Prants, S., Ross, T., Rypina, I. I., Sasai, Y., Trusenkova, O. O., Ustinova, E. I., and Zhong, Y.: Review of oceanic mesoscale processes in the North Pacific: Physical and biogeochemical impacts, *Progress in Oceanography*, 212, 102955, <https://doi.org/10.1016/j.pocean.2022.102955>, 2023.
- Van Meurs, P. and Niiler, P. P.: Temporal variability of the large-scale geostrophic surface velocity in the northeast Pacific, *Journal of physical oceanography*, 27, 2288-2297, [https://doi.org/10.1175/1520-0485\(1997\)027<2288:TVOTLS>2.0.CO;2](https://doi.org/10.1175/1520-0485(1997)027<2288:TVOTLS>2.0.CO;2), 1997.
- 590 Wunsch, C.: Patterns of kinetic energy conversion in a time-average upper ocean, *Progress in Oceanography*, 234, 103453, <https://doi.org/10.1016/j.pocean.2025.103453>, 2025.



- Xie, C., Gao, A.-K., and Lu, X.: Global Estimation of Subsurface Eddy Kinetic Energy of Mesoscale Eddies Using a Multiple-input Residual Neural Network, arXiv, <https://doi.org/10.48550/arXiv.2412.10656>, 2024.
- 595 Zhang, W., Griffies, S. M., Hallberg, R. W., Kuo, Y.-H., and Wolfe, C. L. P.: The Role of Surface Potential Vorticity in the Vertical Structure of Mesoscale Eddies in Wind-Driven Ocean Circulations, *Journal of Physical Oceanography*, 54, 1243-1266, <https://doi.org/10.1175/JPO-D-23-0203.1>, 2024.
- Zhang, Z., Qiu, B., Klein, P., and Travis, S.: The influence of geostrophic strain on oceanic ageostrophic motion and surface chlorophyll, *Nature Communications*, 10, 2838, <https://doi.org/10.1038/s41467-019-10883-w>, 2019.
- 600 Zhou, X., Zhu, S., Jia, W., and Yao, H.: Estimating Subsurface Thermohaline Structure in the Tropical Western Pacific Using DO-ResNet Model, *Atmosphere*, 15, <https://doi.org/10.3390/atmos15091043>, 2024.